

ASTROMETRIC AND PHOTOMETRIC DATA FUSION FOR INACTIVE SPACE OBJECT MASS AND AREA ESTIMATION

Richard Linares

University at Buffalo, State University of New York, Amherst, NY, 14260-4400

linares2@buffalo.edu

Moriba K. Jah

Air Force Research Laboratory, Kirtland AFB, New Mexico, 87117

AFRL.RVSV@Kirtland.af.mil

John L. Crassidis

University at Buffalo, State University of New York, Amherst, NY, 14260-4400

johnc@buffalo.edu

Fred A. Leve

Air Force Research Laboratory, Kirtland AFB, New Mexico, 87117

AFRL.RVSV@Kirtland.af.mil

Tom Kececy

The Boeing Company, Boeing LTS, Colorado Springs, CO, 80919

thomas.m.kececy@boeing.com

Abstract

This paper presents a new method to determine the mass of an inactive space object from the fusion of photometric and astrometric data. Typically, the effect of solar radiation pressure is used to determine area-to-mass ratio for space objects from angles observations. The area-to-mass ratio of a space object can greatly affect its orbital dynamics. As a consequence, angles data are sensitive to this quantity. On the other hand, photometric data is not sensitive to mass but is a strong function of the albedo-area and the rotational dynamics of the space object. The albedo-area can be used to determine the amount of energy reflected from solar radiation. Since these two data types are sensitive to albedo-area and area-to-mass, then through fusion of photometric data with angles data it is possible to determine the area and mass of a space object. This work employs an unscented Kalman filter to estimate rotational and translational states, area and mass of an inactive space object. Mass is not observable with only angles data or only photometric data alone, but it is shown in this work that with the two combined data types mass can be recovered. Recovery of space object characteristics and attitude and orbit trajectories with sufficient accuracy is demonstrated in this paper via simulation.

1 Introduction

Deep space optical surveys of near geosynchronous (GEO) objects have identified a class of high area-to-mass ratio (HAMR) objects [1]. The exact characteristics of these objects are not well known and their motion pose a collision hazard with GEO objects due to the SRP induced, large variations of inclination and eccentricity. These objects are typically non-resolved and difficult to track due to dim magnitude and dynamic mis-modeling. Therefore, characterizing the large population of HAMR objects in geostationary orbit is required to allow for a better understanding of their origins, and the current and future threats they pose to the active SO population.

Light curves (i.e., the SO temporal brightness as seen from the observer) have been used to estimate the shape for an object. In particular, light curve approaches have been studied to estimate the shape and state of asteroids [2, 3]. Reference [4] uses light curves and thermal emissions to recover the three-dimensional shape of an object assuming its orientation with respect to the observer is known. The benefits of using a light curve-based approach over the aforementioned others is that it is not limited to larger objects in lower altitudes, and it can be applied to small and dim objects in higher altitudes, such as geosynchronous orbits. Here light curve data is considered for mass estimation, which is also useful since it provides a mechanism to estimate both position and attitude, as well as their respective rates [5, 6].

Estimating the dynamic characteristics of a HAMR object using light curve and astrometric data can allow for mass parameters to be observable. Estimating mass for HAMR objects can help in the development of a detailed understanding of the origin and dynamics of these objects. It has been shown that the SRP albedo area-to-mass ratio, $\frac{C_{rA}}{m}$, is observable from angles data [7] through the dynamic mis-modeling of SRP forces. The term mis-modeling represents the inappropriate modeling of the force model and this mis-modeling produces a difference between observations and prediction. These differences allow for parameters to be estimated. Reference [7] conducts a study with simulated and actual data to quantify the error in the estimates of $\frac{C_{rA}}{m}$ and good performance is found using data spanning over a number of months. Also Ref. [8] shows that orbital, attitude and shape parameters can be recovered with sufficient accuracy using a multiple-model adaptive estimation approach coupled with an unscented Kalman filter. This approach works reasonably well but requires that the area-to-mass ratio is known *a priori*. The purpose of this work is to show that since $\frac{C_{rA}}{m}$ is observable from angles data and shape/albedo properties are observable from photometric data, then by fusing these data types mass can be extracted with reasonable accuracy.

Filtering algorithms for state estimation, such as the extended Kalman filter (EKF) [9], the unscented Kalman filter (UKF) [10] and particle filters [11] are commonly used to both estimate hidden (indirectly observable) states and filter noisy measurements. The basic difference between the EKF and the UKF results from the manner in which the state distribution of the nonlinear models is approximated. The UKF, introduced by Julier and Uhlmann [10], uses a nonlinear transformation called the unscented transform, in which the state probability density function (pdf) is represented by a set of weighted sigma points (state vectors deterministically sampled about a mean). These are used to parameterize the true mean and covariance of the state distribution. When the sigma points are propagated through the nonlinear system, the posterior mean and covariance are obtained up to the second order for any nonlinearity. The EKF and UKF assume that the process noise terms are represented by zero-mean Gaussian white-noise processes and the measurement noise is represented by zero-mean Gaussian random variable. Furthermore both approaches assume that the *a posteriori* and *a priori* pdf is Gaussian in a linear domain. This is true given the previous assumptions but under the effect of nonlinear measurement functions and system dynamics the initial Gaussian state uncertainty may quickly become non-Gaussian. Both filters only provide approximate solutions to the nonlinear filtering problem, since the *a posteriori* and *a priori* pdf are most often non-Gaussian due to nonlinear effects. The EKF typically works well only in the region where the first-order Taylor-series linearization adequately approximates the non-Gaussian pdf. The UKF provides higher-order moments for the computation of the *a posteriori* pdf without the need to calculate Jacobian matrices as required in the EKF. The light curve measurement model is highly nonlinear, and Jacobian calculations are non-trivial; thus, the UKF is used to provide a numerical means of estimating the states of the SO using light curve measurement models.

Attitude estimation using light curve data has been demonstrated in Ref. [12]. The main goal of this current work is to use light curve data to, autonomously and in near realtime, determine the mass of a SO along with its attitude (rotational) and translational states. In order to accomplish this task, a UKF is designed for state estimation of these quantities. The translational dynamics includes both conservative gravitational and non-conservative SRP. The rotational dynamics includes classic Euler dynamics coupled with SRP torque. Light curve and angles data are employed in the UKF structure to estimate the states.

The organization of this paper is as follows. First, the methods used to recover mass are discussed. Then the models used for SO shape, orbital dynamics and attitude dynamics are discussed. Following this a description of the measurement models used in this paper are given. Next, a review of the UKF approach is provided. Finally, simulation results of the mass and albedo-area estimation approach are provided.

2 Details of the Present Three Approaches

Two approaches are considered in this work: the first approach estimates for albedo-area, $\mathcal{AC}_{\text{diff}}$, which uses an assumed value for the albedo, a , to allow for estimation of mass, and the second approach uses estimated rotational dynamics to infer information about the area and therefore allow information about mass to be gained. Also this work assumes completely diffuse objects and therefore the albedo is equal to $a = C_{\text{diff}}$. As mentioned previously, light curve data is sensitive to $\mathcal{AC}_{\text{diff}}$ and angles data are sensitive to $\frac{C_r \mathcal{A}}{m}$, where C_r is the albedo coefficient for the SRP force [7]. The C_r coefficient is a function of the albedo of the SO; $C_r = 1+r$ for the cannonball model [7] where r is the reflectance coefficient and is a function of the albedo, and therefore, to allow for mass to be separated from area, an estimate of albedo must be determined. It will be shown in §2.3 that $C_r = 1 + \frac{2}{3}C_{\text{diff}}$ for a diffuse sphere assuming Lambert's cosine law and $C_r = 1 + \frac{4}{9}C_{\text{diff}}$ for a diffuse flat plate assuming Lambert's cosine law with the normal direction aligned with the sun direction.

Air Force Maui Optical and Supercomputing site Advance Electro-Optical System (AMOS) researchers have calibrated for nominal albedo by using observations of known SOs to determine effective albedos for different classes of objects [13]. The analysis indicated the best effective albedo and albedo range that provides a 90% confidence range for each object class. NASA and AMOS have jointly determined that, for payloads and rocket-bodies reflecting sunlight, an albedo of $a \approx 0.3$ best reproduces known sizes with a 90% confidence range of $0.1 \leq a \leq 0.7$ [13]. For orbital debris, an effective albedo of $a \approx 0.15$ best reproduces the sizes estimated from radar with a 90% confidence of roughly $0.05 \leq a \leq 0.3$ [13]. Therefore, assuming a value for the albedo that is consistent with observations of a typical SO can provide a means to estimate mass with estimates of albedo-area. The state vector for the joint attitude, position and parameter estimate problem using method I is given by

$$\mathbf{x}_k = \left[\mathbf{q}_I^{B^T} \quad \boldsymbol{\omega}_{B/I}^{B^T} \quad \mathbf{r}^{I^T} \quad \mathbf{v}^{I^T} \quad m \quad \mathcal{AC}_{\text{diff}}^T \right]^T \Big|_{t_k}, \quad (1)$$

where position and velocity of an Earth orbiting SO are denoted by $\mathbf{r}^I = [x \ y \ z]^T$ and $\mathbf{v}^I = [v_x \ v_y \ v_z]^T$, respectively, $\boldsymbol{\omega}_{B/I}^{B^T}$ is the angular velocity of the SO with respect to the inertial frame, and \mathbf{q}_I^B is the quaternion that parameterizes the orientation of the SO with respect to the inertial frame. The mass, m , of the SO is added as a state along with the albedo-area vector, $\mathcal{AC}_{\text{diff}}$, containing the albedo-area of each side of the SO. The benefit of this approach is that since the albedo-area vector is part of the estimated state vector the orientation of the SO is not affected by the uncertainty in the assumed albedo, but rather the assumed albedo is used to compute the SRP force on the SO and in turn estimate the mass of the SO. The SRP force discussed in the following section requires either estimates of area and albedo-area or estimates of albedo-area and albedo. It is noted that using this approach will not affect the estimates of rotational and albedo-area states since the assumed albedo will only be used in the dynamic equations for the SRP force. The uncertainty in the assumed albedo will affect the estimates for mass and translational states since the assumed albedo will be used in the SRP force calculation. In this approach no estimate of the area is directly needed, but the assumed albedo is used in the dynamic state propagation.

The second estimation approach used in this work makes use of the fact that the observation and dynamics are both sensitive to the desired quantities but are not by themselves sensitive to all desired quantities. For example photometric data is sensitive to attitude, angular velocity and the albedo-area of the SO, whereas astrometric data is sensitive to the position, velocity and area-to-mass ratio. The sensitivity of area-to-mass ratio is from the dynamic mis-modeling due to the SRP force, where SRP is also a function of orientation and albedo-area. If we consider a state vector that consists of parameters that are observable from astrometric data and parameters that are observable from photometric data, then it is possible separate area from mass.

The state vector for the joint attitude, position and parameter estimation problem with area states using method II is given by

$$\mathbf{x}_k = \left[\mathbf{q}_I^{B^T} \quad \boldsymbol{\omega}_{B/I}^{B^T} \quad \mathbf{r}^{I^T} \quad \mathbf{v}^{I^T} \quad m \quad \mathcal{AC}_{\text{diff}}^T \quad \mathcal{A}^T \right]^T \Big|_{t_k}, \quad (2)$$

where the states of areas, \mathcal{A} , are added and contain the areas of each side of the SO. The areas and albedo-areas are added as separate states due to the fact that each data type is sensitive to one but not to both. These states have a dependency since the albedo-areas are just products of the albedo a for each side with

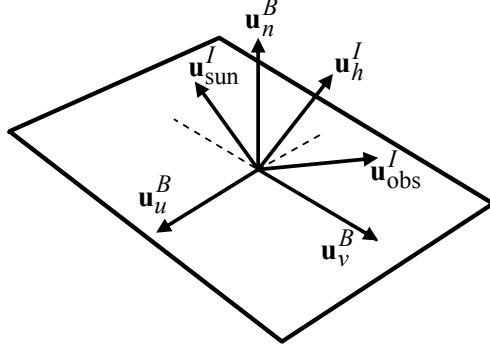


Figure 1: Geometry of Reflection

the respective area for that side. The state vector for the joint attitude, position and parameter estimation problem with albedo states using method III is given by

$$\mathbf{x}_k = \left[\mathbf{q}_I^{B^T} \quad \boldsymbol{\omega}_{B/I}^{B^T} \quad \mathbf{r}^{I^T} \quad \mathbf{v}^{I^T} \quad m \quad \mathcal{A} \mathbf{r}^T \quad \mathbf{C}_{\text{diff}}^{T^T} \right]^T \Big|_{t_k}, \quad (3)$$

2.1 Shape Model

The shape model considered in this work consists of a finite number of flat facets. For curved surfaces this model becomes more accurate as the number of facets is increased. Each facet has a set of three basis vectors $(\mathbf{u}_n^B, \mathbf{u}_u^B, \mathbf{u}_v^B)$ associated with it as defined in Figure 1. The unit vector \mathbf{u}_n^B points in the direction of the outward normal to the facet, and the vectors \mathbf{u}_u^B and \mathbf{u}_v^B are in the plane of the facet. The notation superscript B denotes that the vector is expressed in body coordinates. The SOs are assumed to be rigid bodies, and the unit vectors \mathbf{u}_n^B , \mathbf{u}_u^B and \mathbf{u}_v^B therefore do not change in time since they are expressed in the body frame.

The light curve and the SRP models discussed in the next sections require that these vectors be expressed in inertial coordinates. Since the SO body is rotating, these vectors will change inertially. The body vectors can be rotated to the inertial frame by the standard attitude mapping given by

$$\mathbf{u}_k^B = A(\mathbf{q}_I^B) \mathbf{u}_k^I, \quad k = u, v, n, \quad (4)$$

where $A(\mathbf{q}_I^B)$ is the attitude matrix mapping the inertial frame to the body frame using the quaternion parameterization. The superscript I denotes that a vector is expressed in inertial coordinates. The unit vector $\mathbf{u}_{\text{sun}}^I$ points from the SO to the Sun direction, and the unit vector $\mathbf{u}_{\text{obs}}^I$ points from the SO to the observer as shown in Figure 2. The vector \mathbf{u}_h^I is the normalized half vector between $\mathbf{u}_{\text{sun}}^I$ and $\mathbf{u}_{\text{obs}}^I$ also shown in Figure 2. This vector is also known as the Sun-SO-Observer bisector. Each facet has an area $\mathcal{A}(i)$ associated with it. Once the number of facets has been defined and their basis vectors are known, the areas $\mathcal{A}(i)$ define the size and shape of the SO.

For the development of the measured light curve data, faceted SO rectangular cuboid shape models as shown in Figure 2 are used. The rectangular cuboid model is described by three parameters, l , a , and d , which are the length, width, and height, respectively.

2.2 Rotational and Translational Models

The two-body equations of motion with SRP accelerations are given by

$$\ddot{\mathbf{r}}^I = -\frac{\mu}{r^3} \mathbf{r}^I + \mathbf{a}_{\text{srp}}^I, \quad (5)$$

where μ is the gravitational parameter of the Earth, $r = \|\mathbf{r}^I\|$, and $\mathbf{a}_{\text{srp}}^I$ represents the acceleration perturbation due to SRP, which will be discussed in detail in the following section.

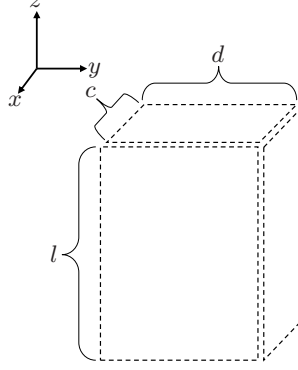


Figure 2: Cuboid Shape Model

A number of parameterizations exist to specify attitude, including Euler angles, quaternions and Rodriguez parameters [14]. This paper uses the quaternion, which is based on the Euler angle/axis parametrization. The quaternion is defined as $\mathbf{q} \equiv [\boldsymbol{\rho}^T \ q_4]^T$ with $\boldsymbol{\rho} = \hat{\mathbf{e}} \sin(\nu/2)$, and $q_4 = \cos(\nu/2)$, where $\hat{\mathbf{e}}$ and ν are the Euler axis of rotation and rotation angle, respectively. The quaternion must satisfy a unit norm constraint, $\mathbf{q}^T \mathbf{q} = 1$. In terms of the quaternion, the attitude matrix is given by

$$A(\mathbf{q}) = \Xi^T(\mathbf{q})\Psi(\mathbf{q}), \quad (6)$$

where

$$\Xi(\mathbf{q}) \equiv \begin{bmatrix} q_4 I_{3 \times 3} + [\boldsymbol{\rho} \times] \\ -\boldsymbol{\rho}^T \end{bmatrix} \quad (7a)$$

$$\Psi(\mathbf{q}) \equiv \begin{bmatrix} q_4 I_{3 \times 3} - [\boldsymbol{\rho} \times] \\ -\boldsymbol{\rho}^T \end{bmatrix}, \quad (7b)$$

with

$$[\mathbf{a} \times] \equiv \begin{bmatrix} 0 & -a_3 & a_2 \\ a_3 & 0 & -a_1 \\ -a_2 & a_1 & 0 \end{bmatrix}, \quad (8)$$

for any general 3×1 vector \mathbf{a} defined such that $[\mathbf{a} \times] \mathbf{b} = \mathbf{a} \times \mathbf{b}$.

The rotational dynamics are given by the coupled first-order differential equations:

$$\dot{\mathbf{q}}_I^B = \frac{1}{2} \Xi(\mathbf{q}_I^B) \boldsymbol{\omega}_{B/I}^B \quad (9a)$$

$$\dot{\boldsymbol{\omega}}_{B/I}^B = J_{\text{SO}}^{-1} \left(\mathbf{T}_{\text{srp}}^B - [\boldsymbol{\omega}_{B/I}^B \times] J_{\text{SO}} \boldsymbol{\omega}_{B/I}^B \right), \quad (9b)$$

where J_{SO} is the inertia matrix of the SO and $\mathbf{T}_{\text{srp}}^B$ is the net torque acting on the SO due to SRP expressed in body coordinates. The SO is assumed to be of uniform density, and therefore the principal components of the inertia tensor for the shape model discussed in §2.1 and given in Figure 2 are given by

$$J_1 = m \frac{c^2 + b^2}{12} \quad (10a)$$

$$J_2 = m \frac{c^2 + l^2}{12}, \quad (10b)$$

$$J_3 = m \frac{l^2 + b^2}{12}, \quad (10c)$$

where m is the mass of the SO and c , l , and d are the shape parameters defined in Figure 2.

2.3 Solar Radiation Force Model

For higher altitude objects ($\geq 1,000$ km) SRP represents the primary non-conservative perturbation acting on SOs. Because SRP depends upon the SO's position and orientation, the position and attitude dynamics are thus coupled. The acceleration due to SRP is computed as a function of the total solar energy impressed upon exposed SO surfaces that are reflected, absorbed and reradiated. The rate at which radiant energy is incident on an element of area $d\mathcal{A}$ is a function of angle between the normal to $d\mathcal{A}$, \mathbf{u}_n , and the Sun direction \mathbf{u}_{sun} . The power of incident radiant energy is given by

$$P_I = \frac{\Phi_{\text{sun,tot}}}{(d/d_0)^2} (\mathbf{u}_n \cdot \mathbf{u}_{\text{sun}}) d\mathcal{A}, \quad (11)$$

where $\Phi_{\text{sun,tot}}$ is the average incident radiant flux density from the Sun at 1 AU, given by $\Phi_{\text{sun,tot}} = 1,367$ W/m². Therefore the energy flux at any distance d is given by $\Phi_{\text{sun,tot}}/(d/d_0)^2$ where $d_0 = 1$ AU. The reflected radiation will have the following diffuse and specular power:

$$P_D = C_{\text{diff}} \frac{\Phi_{\text{sun,tot}}}{(d/d_0)^2} (\mathbf{u}_n \cdot \mathbf{u}_{\text{sun}}) d\mathcal{A} \quad (12a)$$

$$P_S = C_{\text{spec}} \frac{\Phi_{\text{sun,tot}}}{(d/d_0)^2} (\mathbf{u}_n \cdot \mathbf{u}_{\text{sun}}) d\mathcal{A}, \quad (12b)$$

where the incident solar radiant energy is accounted for in three terms: the absorbed energy, C_{abs} , the specularly reflected energy C_{spec} , and the diffusely reflected energy, C_{diff} , which yields

$$C_{\text{abs}} + C_{\text{spec}} + C_{\text{diff}} = 1. \quad (13)$$

The elemental force on $d\mathcal{A}$ can be written in three terms: incident force, \mathbf{dF}_I , specular reflection force, \mathbf{dF}_S , and diffuse reflection force, \mathbf{dF}_D . The incident force accounts for force due to the three terms C_{abs} , C_{spec} , and C_{diff} , since for each term the radiant particle is at least brought to rest before being absorbed or reflected. Therefore, \mathbf{dF}_I accounts for the transfer in momentum to bring a radiated particle to rest. The force term for diffuse and specular reflectance accounts for the momentum transfer due to reflection. The momentum contribution due to incident energy is in the opposite direction of the normal, given by

$$\mathbf{dF}_I = -\frac{P_I}{c} \mathbf{u}_n. \quad (14)$$

The force exerted by specularly reflected energy is in the direction of specular reflection which is given by reflecting the vector \mathbf{u}_{sun} about an axis defined by the direction \mathbf{u}_n . Then the force exerted by specular reflection is given by

$$\mathbf{dF}_S = \frac{P_S}{c} [2 (\mathbf{u}_n \cdot \mathbf{u}_{\text{sun}}) \mathbf{u}_n - \mathbf{u}_{\text{sun}}]. \quad (15)$$

Diffusely reflected energy will reflect equally in all directions and the resulting force will be in the normal direction due to symmetric components canceling out. For surfaces obeying Lambert's cosine law of diffuse emission the diffuse term will be [15]

$$\mathbf{dF}_D = \frac{2}{3} \frac{P_D}{c} \mathbf{u}_n, \quad (16)$$

where the factor $\frac{2}{3}$ accounts for the portion of energy that is reflected in the normal direction. Then the force on an element of area is given by

$$\mathbf{dF} = \mathbf{dF}_I + \mathbf{dF}_S + \mathbf{dF}_D. \quad (17)$$

The force acting on a body due to solar radiation pressure can be determined by integrating over the Sun exposed surface area, given by

$$\mathbf{F} = \int_{\text{sun}} (\mathbf{dF}_I + \mathbf{dF}_S + \mathbf{dF}_D). \quad (18)$$

For a spherical body this integral is calculated over the Sun exposed area. The result is given by

$$\mathbf{F} = -\frac{\Phi_{\text{sun,tot}}}{c(d/d_0)^2} \mathcal{A} \left[1 + \frac{2}{3} C_{\text{diff}} \right] \mathbf{u}_{\text{sun}}. \quad (19)$$

This equation can be rewritten in terms of albedo

$$\mathbf{F} = -\frac{\Phi_{\text{sun,tot}}}{c(d/d_0)^2} \mathcal{A} C_r \mathbf{u}_{\text{sun}}, \quad (20)$$

where $C_r = 1 + \frac{2}{3}C_{\text{diff}}$. Similarly the forces can be calculated for a flat plate:

$$\begin{aligned} \mathbf{F} = & -\frac{\Phi_{\text{sun,tot}}}{c(d/d_0)^2} \mathcal{A} (\mathbf{u}_n \cdot \mathbf{u}_{\text{sun}}) \left[(1 - C_{\text{spec}}) \mathbf{u}_n \right. \\ & \left. + \left(\frac{4}{9}C_{\text{diff}} + 2C_{\text{spec}} (\mathbf{u}_n \cdot \mathbf{u}_{\text{sun}}) \right) \mathbf{u}_{\text{sun}} \right] \end{aligned} \quad (21)$$

Under the assumption of a perfectly diffuse flat plate, Eq. (21) becomes

$$\mathbf{F} = -\frac{\Phi_{\text{sun,tot}}}{c(d/d_0)^2} (\mathbf{u}_n \cdot \mathbf{u}_{\text{sun}}) \left[\mathcal{A} \mathbf{u}_n + \frac{4}{9} \mathcal{A} C_{\text{diff}} \mathbf{u}_{\text{sun}} \right]. \quad (22)$$

We can note that, if \mathbf{u}_n remains aligned with \mathbf{u}_{sun} , a similar expression to Eq. (20) can be written for the flat plate model, where $C_r = 1 + \frac{4}{9}C_{\text{diff}}$ in the case of the flat plate. To calculate the SRP force for the facet model discussed in §2.1, the SRP force is calculated for each facet using the SRP force equation for a flat plate, Eq. (22), and then summed over all facets to obtain the total SRP force on the body:

$$\mathbf{F}_{\text{srp}}^I = \sum_{j=1}^{N_F} \mathbf{F}_{\text{srp},j}^I, \quad (23)$$

where N_F is the total number of facets. The sum is performed over all sides of the SO. If for any side the angle between the surface normal and the Sun's direction is greater than $\pi/2$, then this side is not facing the Sun and receives no energy from the Sun. Therefore, the solar radiation pressure for these sides is set to zero, $\mathbf{F}_{\text{srp},j}^I = \mathbf{0}$ if $\theta_{\text{inc}} > \pi/2$. The acceleration due to SRP is then simply given by $\mathbf{a}_{\text{srp}}^I = \mathbf{F}_{\text{srp}}^I/m$.

The solar radiation pressure moments can be calculated by assuming that the SRP force acts through the center of each facet. Then the SRP moments can be written as

$$\mathbf{T}_{\text{srp}}^B = \sum_{j=1}^{N_F} [\mathbf{r}_i^B \times] \mathcal{A} \mathbf{F}_{\text{srp},j}^B, \quad (24)$$

where \mathbf{r}_i^B is the location of the geometric center of each facet with respect to the center of mass of the SO in body coordinates. The SRP moments are used with Eq. (9) to simulate the rotational dynamics of the SO.

2.4 Observation Model

Consider observations made by an optical site which measures azimuth and elevation to a SO. The geometry and common terminology associated with this observation is shown in Figure 3, where \mathbf{d}^I is the position vector from the observer to the SO, \mathbf{r}^I is the position of the SO in inertial coordinates, \mathbf{R}^I is the radius vector locating the observer, α and δ are the right ascension and declination of the SO, respectively, θ is the sidereal time of the observer, λ is the latitude of the observer, and ϕ is the East longitude from the observer to the SO. The fundamental observation is given by

$$\mathbf{d}^I = \mathbf{r}^I - \mathbf{R}^I. \quad (25)$$

In non-rotating equatorial (inertial) components the vector \mathbf{d}^I is given by

$$\mathbf{d}^I = \begin{bmatrix} x - \|\mathbf{R}^I\| \cos(\theta) \cos(\lambda) \\ y - \|\mathbf{R}^I\| \sin(\theta) \cos(\lambda) \\ z - \|\mathbf{R}^I\| \sin(\lambda) \end{bmatrix}. \quad (26)$$

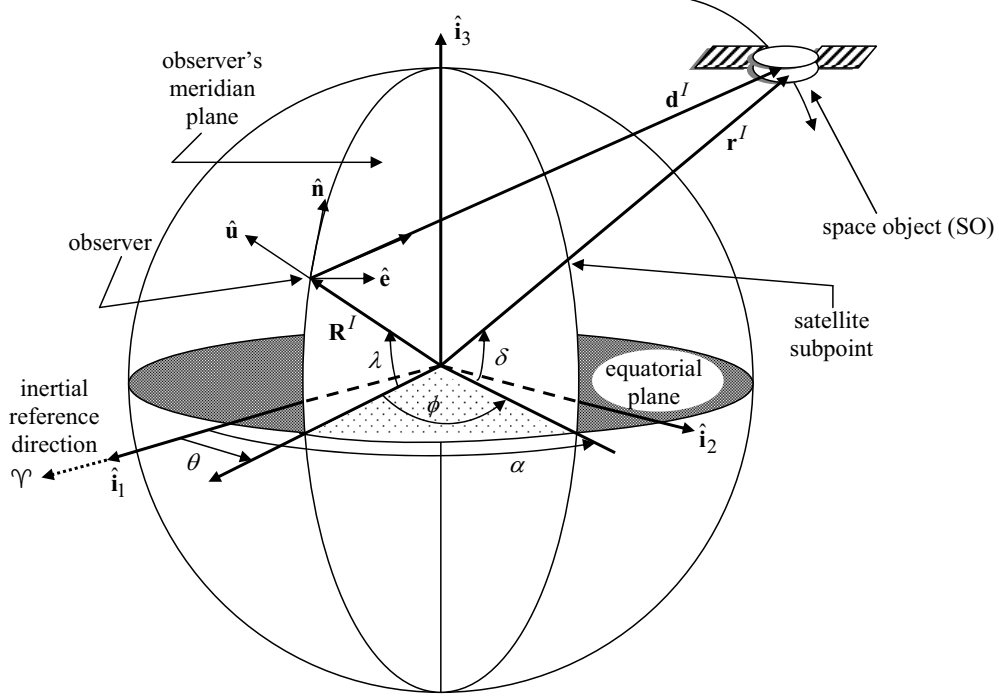


Figure 3: Geometry of Earth Observations of Spacecraft Motion

The conversion of \mathbf{d}^I from the inertial to the observer coordinate system (Up-East-North) is given by

$$\begin{bmatrix} \rho_u \\ \rho_e \\ \rho_n \end{bmatrix} = \begin{bmatrix} \cos(\lambda) & 0 & \sin(\lambda) \\ 0 & 1 & 0 \\ -\sin(\lambda) & 0 & \cos(\lambda) \end{bmatrix} \times \begin{bmatrix} \cos(\theta) & \sin(\theta) & 0 \\ -\sin(\theta) & \cos(\theta) & 0 \\ 0 & 0 & 1 \end{bmatrix} \mathbf{d}^I. \quad (27)$$

The angle observations consist of the azimuth, az, and elevation, el. The observation equations are given by

$$\text{az} = \tan^{-1} \left(\frac{\rho_e}{\rho_n} \right) \quad (28a)$$

$$\text{el} = \sin^{-1} \left(\frac{\rho_u}{\|\mathbf{d}^I\|} \right). \quad (28b)$$

In addition to the azimuth and elevation, the optical site also records the magnitude of the brightness of the SO. The brightness of an object in space can be modeled using an Phong light diffusion model [15]. This model is based on the bidirectional reflectance distribution function (BRDF) which models light distribution scattered from the surface due to the incident light. The BRDF at any point on the surface is a function of two directions, the direction from which the light source originates and the direction from which the scattered light leaves the observed surface. The model in Ref. [15] decomposes the BRDF into a specular component and a diffuse component. The two terms sum to give the total BRDF:

$$\rho_{\text{total}}(i) = \rho_{\text{spec}}(i) + \rho_{\text{diff}}(i). \quad (29)$$

The diffuse component represents light that is scattered equally in all directions (Lambertian) and the specular component represents light that is concentrated about some direction (mirror-like). Reference [15] develops a model for continuous arbitrary surfaces but simplifies for flat surfaces. This simplified model is employed in this work as shape models that are considered to consist of a finite number of flat facets. Therefore the total observed brightness of an object becomes the sum of the contribution from each facet.

Under the flat plate assumption the specular term of the BRDF becomes [15]

$$\rho_{\text{spec}}(i) = C_{\text{spec}} \frac{(\mathbf{u}_{\text{obs}} \cdot \mathbf{u}_{\text{spec}})^\alpha}{(\mathbf{u}_{\text{sun}} \cdot \mathbf{u}_n)}, \quad (30)$$

where the parameter α defines the width of the specular lobe. The vector \mathbf{u}_{spec} is the direction of specular reflection and is defined as $\mathbf{u}_{\text{spec}} = 2(\mathbf{u}_n \cdot \mathbf{u}_{\text{sun}})\mathbf{u}_n - \mathbf{u}_{\text{sun}}$. The diffuse term of the BRDF is

$$\rho_{\text{diff}}(i) = \frac{C_{\text{diff}}}{\pi}. \quad (31)$$

The apparent magnitude of a SO is the result of sunlight reflecting off of its surfaces along the line-of-sight to an observer. First, the fraction of visible sunlight that strikes an object (and is not absorbed) is computed by

$$F_{\text{sun}}(i) = \Phi_{\text{sun,vis}} \rho_{\text{total}}(i) (\mathbf{u}_n^I(i) \cdot \mathbf{u}_{\text{sun}}^I), \quad (32)$$

where $\Phi_{\text{sun,vis}} = 455 \text{ W/m}^2$ is the power per square meter impinging on a given object due to visible light striking the surface. If either the angle between the surface normal and the observer's direction or the angle between the surface normal and Sun direction is greater than $\pi/2$, then there is no light reflected toward the observer. If this is the case then the fraction of visible light is set to $F_{\text{sun}}(i) = 0$.

Next, the fraction of sunlight that strikes an object that is reflected must be computed:

$$F_{\text{obs}}(i) = \frac{F_{\text{sun}}(i) \mathcal{A}(i) (\mathbf{u}_n^I(i) \cdot \mathbf{u}_{\text{obs}}^I)}{\|\mathbf{d}^I\|^2}. \quad (33)$$

The reflected light is now used to compute the apparent brightness magnitude, which is measured by an observer:

$$m_{\text{app}} = -26.7 - 2.5 \log_{10} \left| \sum_{i=1}^{N_F} \frac{F_{\text{obs}}(i)}{\Phi_{\text{sun,vis}}} \right|, \quad (34)$$

where -26.7 is the apparent magnitude of the Sun.

3 Unscented Kalman Filter Formulation

The unscented Kalman filter (UKF) is chosen for state estimation because it has at least the accuracy of a second-order filter [10] without the requirement of computing Jacobians like the EKF. The UKF structure is used for estimating rotational, translational, and parameter states based on fusing angles and light curve data along with their associated models as discussed in §2. The attitude UKF described in Ref. [16] is used in the same manner as the one shown in Refs. [5] and [12].

Applying the UKF structure for attitude estimation has some challenges. For instance, although three parameter sets are attitude minimal representations, they inherently have singularities. On the other hand the quaternion representation, which is a four parameter set with no singularity, has a nonlinear constraint which results in a singular covariance matrix. In addition, the quaternion is not constitute by directly adding quaternions but through quaternion multiplication. This does not allow use of quaternions in a straightforward UKF implementation. Reference [16] overcomes these challenges by utilizing generalized Rodrigues parameters (GRPs), a three parameter set, to define the local error and quaternions to define the global attitude.

The global parameterization for attitude UKF approach used for this work is the quaternion while a minimal parametrization involving the generalized Rodrigues parameters (GRPs) is used to define the local error. The representation of the attitude error as a GRP is useful for the propagation and update stages of the attitude covariance because the structure of the UKF can be used directly. Complete explanations of the quaternion and its mapping to GRPs is provided in Refs. [14] and [17]. In the UKF implementation described in Ref. [16], the covariance matrix is interpreted as the covariance of the error GRP because for small angle errors, the error GRP is additive and the UKF structure can be used directly to compute sigma-points. The error GRP sigma points are converted to error quaternions and then to global quaternions for the propagation stage. To compute the propagated covariance the global quaternions are converted to error quaternions and then back to error GRPs. The process is then as follows: error GRP \rightarrow error quaternion, error quaternion \rightarrow global quaternion, global quaternion \rightarrow error quaternion, and finally error quaternion \rightarrow error GRP.

3.1 Model and Measurement Uncertainty

A UKF is now summarized for estimating the state of a SO's position, velocity, orientation, rotation rate, mass, albedo-areas and areas given by $\mathbf{x} = [\mathbf{q}_I^{B^T} \ \boldsymbol{\omega}_{B/I}^{B^T} \ \mathbf{r}^{I^T} \ \mathbf{v}^{I^T} \ m \ \mathbf{C}_{\text{diff}} \mathcal{A}^T]^T$ for method I, $\mathbf{x} = [\mathbf{q}_I^{B^T} \ \boldsymbol{\omega}_{B/I}^{B^T} \ \mathbf{r}^{I^T} \ \mathbf{v}^{I^T} \ m \ \mathbf{C}_{\text{diff}} \mathcal{A}^T \ \mathcal{A}^T]^T$ for method II, and $\mathbf{x} = [\mathbf{q}_I^{B^T} \ \boldsymbol{\omega}_{B/I}^{B^T} \ \mathbf{r}^{I^T} \ \mathbf{v}^{I^T} \ m \ \mathbf{C}_{\text{diff}}^T \ \mathcal{A}^T]^T$ for method III. The dynamic models from Eqs. (5) and (9) can be written in the general state equation which gives the deterministic part of the stochastic model:

$$\dot{\mathbf{x}} = \mathbf{f}(\mathbf{x}, t) + G(\mathbf{x}, t) \boldsymbol{\Gamma}(t), \quad (35)$$

where $\boldsymbol{\Gamma}(t)$ is a Gaussian white noise process term with correlation function $Q\delta(t_1 - t_2)$, and $G(\mathbf{x}, t)$ is the process noise influence matrix. The function $\mathbf{f}(\mathbf{x}, t)$ is a general nonlinear function. To solve the general nonlinear filtering problem the UKF utilizes the unscented transformation to determine the mean and covariance propagation through the function $\mathbf{f}(\mathbf{x}, t)$. The dynamic function used in this work consists of rotational and translational dynamics given by the sigma points, which are propagated through the system dynamics:

$$\mathbf{f}([\boldsymbol{\chi}, \hat{\mathbf{q}}]) = \begin{bmatrix} \frac{1}{2} \Xi(\hat{\mathbf{q}}) \hat{\boldsymbol{\omega}}_{B/I}^B \\ J_{\text{SO}}^{-1} \left(\hat{\mathbf{T}}_{\text{srp}}^B - \begin{bmatrix} \hat{\boldsymbol{\omega}}_{B/I}^B \times \\ \hat{\mathbf{v}}^I \end{bmatrix} J_{\text{SO}} \hat{\boldsymbol{\omega}}_{B/I}^B \right) \\ -\frac{\mu}{r^3} \hat{\mathbf{r}}^I + \hat{\mathbf{a}}_{\text{SRP}}^I \end{bmatrix}. \quad (36)$$

If the initial pdf $p(\mathbf{x}_o)$ that describes the associated state uncertainty is given, the solution for the time evolution of $p(\mathbf{x}, t)$ constitutes the nonlinear filtering problem.

Given a system model with initial state and covariance values, the UKF propagates the state vector and the error-covariance matrix recursively. At discrete observation times, the UKF updates the state and covariance matrix conditioned on the information gained from the measurements. The prediction phase is important for overall filter performance. In general, the discrete measurement equation can be expressed for the filter as

$$\tilde{\mathbf{y}}_k = \mathbf{h}(\mathbf{x}_k, t_k) + \mathbf{v}_k, \quad (37)$$

where $\tilde{\mathbf{y}}_k$ is a measurement vector and \mathbf{v}_k is the measurement noise, which is assumed to be a zero-mean Gaussian process with covariance R_k .

All random variables in the UKF are assumed to be Gaussian random variables and their distribution are approximated by the deterministically selected sigma points. The sigma points are selected to be along the principal axis directions of the state error-covariance. Given an $L \times L$ error-covariance matrix P_k , the sigma points are constructed by

$$\boldsymbol{\sigma}_k \leftarrow 2L \text{ columns from } \pm \sqrt{(L + \lambda)P_k} \quad (38a)$$

$$\boldsymbol{\chi}_k(0) = \boldsymbol{\mu}_k \quad (38b)$$

$$\boldsymbol{\chi}_k(i) = \boldsymbol{\sigma}_k(i) + \boldsymbol{\mu}_k, \quad (38c)$$

where \sqrt{M} is shorthand notation for a matrix Z such that $M = Z Z^T$. Given that these points are selected to represent the distribution of the state vector, each sigma point is given a weight that preserves the information contained in the initial distribution:

$$W_0^{\text{mean}} = \frac{\lambda}{L + \lambda} \quad (39a)$$

$$W_0^{\text{cov}} = \frac{\lambda}{L + \lambda} + (1 - \alpha^2 + \beta) \quad (39b)$$

$$W_i^{\text{mean}} = W_i^{\text{cov}} = \frac{1}{2(L + \lambda)}, \quad i = 1, 2, \dots, 2L, \quad (39c)$$

where $\lambda = \alpha^2(L + \kappa) - L$ is a composite scaling parameter.

The constant α controls the spread of the sigma point distribution and should be a small number, $0 < \alpha \leq 1$. $\kappa = 3 - L$ provides an extra degree of freedom that is used to fine-tune the higher-order

moments, and β is used to incorporate prior knowledge of the distribution by weighting the mean sigma point in the covariance calculation.

The reduced state vector, with the error GRP states and the full state vector, with quaternion state vector, for the joint attitude and position estimate problem of method I, are given by

$$\hat{\mathbf{x}}_k^{\delta p} = \begin{bmatrix} \delta \hat{\mathbf{p}} \\ \hat{\boldsymbol{\omega}}_{B/I}^B \\ \hat{\mathbf{r}}^I \\ \hat{\mathbf{v}}^I \\ m \\ \mathbf{C}_{\text{diff}} \mathcal{A} \end{bmatrix}_{t_k}, \quad \hat{\mathbf{x}}_k^q = \begin{bmatrix} \hat{\mathbf{q}}_I^B \\ \hat{\boldsymbol{\omega}}_{B/I}^B \\ \hat{\mathbf{r}}^I \\ \hat{\mathbf{v}}^I \\ m \\ \mathbf{C}_{\text{diff}} \mathcal{A} \end{bmatrix}_{t_k}, \quad (40)$$

where $\delta \hat{\mathbf{p}}$ is the error GRP states associated with the quaternion $\hat{\mathbf{q}}_I^B$ and $\hat{\cdot}$ is used to denote estimate. The initial estimate $\hat{\mathbf{x}}_0$ is the mean sigma point and is denoted $\boldsymbol{\chi}_0(0)$. The error GRP state of the initial estimate is set to zero, while the rest of the states are initialized by their respective initial estimates.

3.2 Using Quaternions for UKF

The error quaternion, denoted by $\delta \mathbf{q}_k^-(i)$, associated with the i^{th} error GRP sigma point is computed by [16]

$$\delta \boldsymbol{\rho}_k^-(i) = f^{-1} [a + \delta q_{4k}^-(i)] \boldsymbol{\chi}_k^{\delta p}(i) \quad (41a)$$

$$\delta q_{4k}^-(i) = \frac{-a \|\boldsymbol{\chi}_k^{\delta p}(i)\|^2 + f \sqrt{f^2 + (1 - a^2) \|\boldsymbol{\chi}_k^{\delta p}(i)\|^2}}{f^2 + \|\boldsymbol{\chi}_k^{\delta p}(i)\|^2} \quad (41b)$$

$$\delta \mathbf{q}_k^-(i) = \begin{bmatrix} \delta \boldsymbol{\rho}_k^-(i) \\ \delta q_{4k}^-(i) \end{bmatrix}, \quad (41c)$$

where a is a parameter from 0 to 1 and f is a scale factor, which is often set to $f = 2(a + 1)$. Here it is noted that the subscript I and superscript B in \mathbf{q}_I^B and its estimates are omitted in this section for brevity. The representation of the attitude estimate perturbed by the i^{th} error quaternion is computed using the quaternion composition:

$$\hat{\mathbf{q}}_k^-(i) = \delta \mathbf{q}_k^-(i) \otimes \hat{\mathbf{q}}_k^-(0), \quad (42)$$

where

$$\mathbf{q}' \otimes \mathbf{q} = [\Psi(\mathbf{q}') \quad \mathbf{q}'] \mathbf{q}. \quad (43)$$

This forms the global quaternion, and the error quaternions corresponding to each propagated quaternion sigma point are computed through the quaternion composition:

$$\delta \mathbf{q}_{k+1}^-(i) = \hat{\mathbf{q}}_{k+1}^-(i) \otimes [\hat{\mathbf{q}}_{k+1}^-(0)]^{-1}, \quad (44)$$

where the notation for the inverse quaternion is defined as:

$$\mathbf{q}^{-1} \equiv \begin{bmatrix} -\boldsymbol{\rho} \\ q_4 \end{bmatrix}. \quad (45)$$

Using the result of Eq. (44), the error GRP sigma points are computed as

$$\delta \mathbf{p}_{k+1}^-(i) = f \frac{\delta \boldsymbol{\rho}_{k+1}^-(i)}{a + \delta q_{4k+1}^-(i)}. \quad (46)$$

Angles data can be used to determine the unknown position and velocity of a SO but if the position is coupled with the attitude dynamics then angles data can assist with attitude estimation as well. However if position is known accurately, then using only light curve data is sufficient to determine the orientation.

Table 1: UKF for Rotational, Translational, and Parameter States

Initialize with $\hat{\mathbf{x}}_o^{\delta\mathbf{p}} = E\{\mathbf{x}_o^{\delta\mathbf{p}}\} \quad \hat{\mathbf{x}}_o^{\mathbf{q}} = E\{\mathbf{x}_o\} \quad \mathbf{P}_o^{\delta\mathbf{p}} = E\{(\mathbf{x}_o^{\delta\mathbf{p}} - \hat{\mathbf{x}}_o^{\delta\mathbf{p}})(\mathbf{x}_o^{\delta\mathbf{p}} - \hat{\mathbf{x}}_o^{\delta\mathbf{p}})^T\}$
Calculate GRP Sigma Points $\boldsymbol{\chi}_k^{\delta\mathbf{p}} = \begin{bmatrix} \hat{\mathbf{x}}_k^{\delta\mathbf{p}} & \hat{\mathbf{x}}_k^{\delta\mathbf{p}} + \gamma\sqrt{P_{k-1}} & \hat{\mathbf{x}}_k^{\delta\mathbf{p}} - \gamma\sqrt{P_{k-1}} \end{bmatrix}$ Calculate Quaternion Sigma Points $\boldsymbol{\chi}_k^{\mathbf{q}} = \begin{bmatrix} \hat{\mathbf{x}}_k^{\mathbf{q}} & \hat{\mathbf{x}}_k^{\mathbf{q}} + \gamma\sqrt{P_{k-1}} & \hat{\mathbf{x}}_k^{\mathbf{q}} - \gamma\sqrt{P_{k-1}} \end{bmatrix}$
Propagate Quaternion Sigma Points $\boldsymbol{\chi}_k^{\mathbf{q}} = \mathbf{f}[\boldsymbol{\chi}_{k-1}^{\mathbf{q}}, t]$ Calculate GRP Sigma Points $\boldsymbol{\chi}_k^{\delta\mathbf{p}} = \begin{bmatrix} \hat{\mathbf{x}}_k^{\delta\mathbf{p}} & \hat{\mathbf{x}}_k^{\delta\mathbf{p}} + \gamma\sqrt{P_{k-1}} & \hat{\mathbf{x}}_k^{\delta\mathbf{p}} - \gamma\sqrt{P_{k-1}} \end{bmatrix}$
Time update $\hat{\mathbf{x}}_{k+1}^- = \sum_{i=0}^{2L} W_i^{\text{mean}} \boldsymbol{\chi}_{k+1}(i)$ $P_{k+1}^- = \sum_{i=0}^{2L} W_i^{\text{cov}} [\boldsymbol{\chi}_{k+1}(i) - \hat{\mathbf{x}}_{k+1}^-] [\boldsymbol{\chi}_{k+1}(i) - \hat{\mathbf{x}}_{k+1}^-]^T + Q_{k+1}$
Measurement update $\boldsymbol{\gamma}_k(i) = \mathbf{h}[\boldsymbol{\chi}_k(i), \hat{\mathbf{q}}_k^-]$ $\hat{\mathbf{y}}_k^- = \sum_{i=0}^{2L} W_i^{\text{mean}} \boldsymbol{\gamma}_k(i)$ $P_k^{yy} = \sum_{i=0}^{2L} W_i^{\text{cov}} [\boldsymbol{\gamma}_k(i) - \hat{\mathbf{y}}_k^-] [\boldsymbol{\gamma}_k(i) - \hat{\mathbf{y}}_k^-]^T$ $P_k^{vv} = P_k^{yy} + R_k$ $P_k^{xy} = \sum_{i=0}^{2L} W_i^{\text{cov}} [\boldsymbol{\chi}_k(i) - \hat{\mathbf{x}}_k^-] [\boldsymbol{\gamma}_k(i) - \hat{\mathbf{y}}_k^-]^T$ $K_k = P_k^{xy} (P_k^{vv})^{-1}$ $\hat{\mathbf{x}}_k^+ = \hat{\mathbf{x}}_k^- + K_k [\hat{\mathbf{y}}_k - \hat{\mathbf{y}}_k^-]$ $P_k^+ = P_k^- - K_k P_k^{vv} K_k^T$
Quaternion update $\hat{\mathbf{q}}_k^+ = \delta \hat{\mathbf{q}}_k^+ \otimes \hat{\mathbf{q}}_k^-(0)$ Set GRP to zero $\delta \mathbf{p} = [0 \quad 0 \quad 0]^T$

3.3 Constrained UKF

The estimator discussed in this work includes constrained states since the area states are constrained to be positive. To account for these constraints the method from ref. [18] is used. Reference [18] incorporates the information of the constraints in the UKF algorithm by projecting sigma points and estimates onto the constraint boundary when sigma points or estimates are found outside the feasible region. Since $r \geq 0$ we have the following constraints

$$C_{\text{diff}} \mathcal{A} \geq 0 \quad (47a)$$

$$\mathcal{A} \geq 0 \quad (47b)$$

Then if the constraints are violated during, sampling the sigma pointing from covariance matrix, after propagation, or after the update step, the estimates and or sigma points that violate the constraints are projected onto the constraint boundary.

3.4 Summary of UKF

The UKF algorithm is described in Table 1. The process starts by first defining two initial state vectors, one that includes quaternion states and one that includes error GRP states. The error GRP states are initially set to zero. The initial covariance matrix is defined as the initial error covariance for the state vector that includes the GRP states, the translational, rotational and parametric states. The covariance matrix is then

used to form the error GRP sigma points. The error GRP sigma points are converted to quaternion sigma points by creating error quaternions from each error GRP and then multiplying the error quaternion to the initial mean quaternion using quaternion multiplication. If any area states sigma points are found outside the feasible region discussed in §3.3 they are projecting onto the constraint boundary.

Next the quaternion sigma points are propagated through the system dynamics using equation Eq. (36). The estimated acceleration and torque due to SRP are calculated with Eqs. (23) and (24), respectively. After propagating the sigma points, the error GRP states are computed with the propagated quaternion sigma points. Again, if any area states sigma points are found outside the feasible region they are projecting onto the constraint boundary. The propagated mean sigma point quaternion, $\hat{\mathbf{q}}_{k+1}^-(0)$, is computed and stored, and error quaternions corresponding to each propagated quaternion sigma point are computed. The non-attitude sigma points are the propagated non-attitude states.

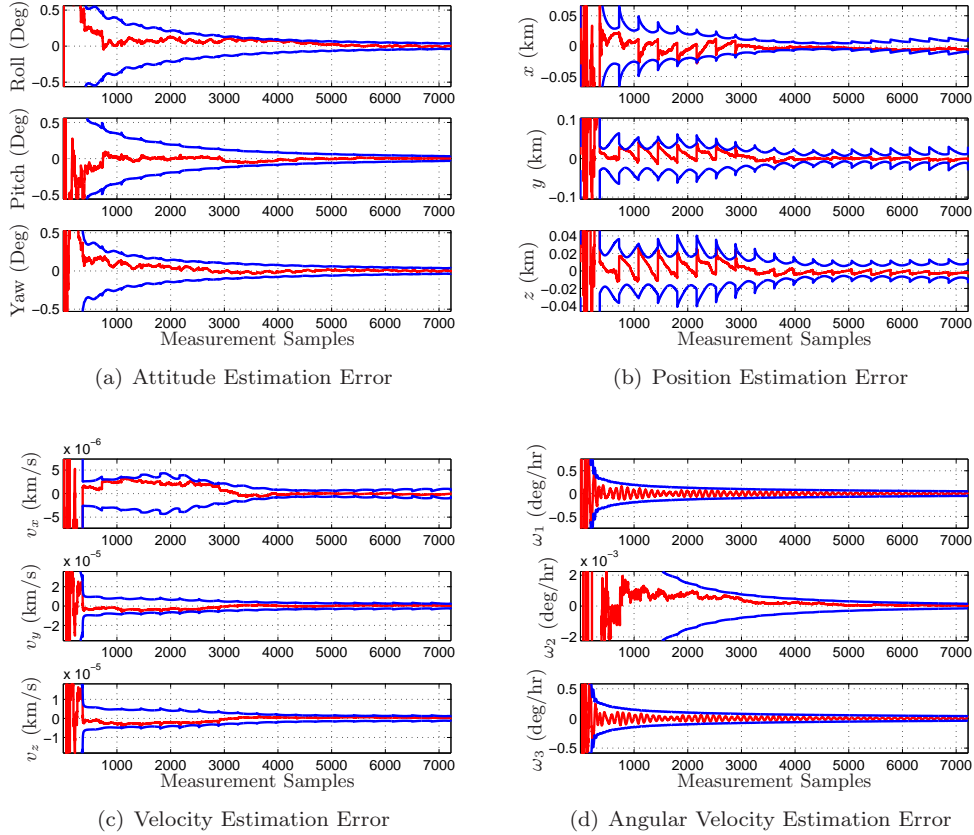


Figure 4: SO State Estimation Results for Method I

After setting the error GRP for the mean sigma point to zero, the propagated sigma points are recombined, and the propagated mean and covariance are calculated as a weighted sum of the sigma points, where Q_{k+1} is the discrete-time process noise covariance. As previously discussed, measurements are available in the form of azimuth, elevation and apparent brightness magnitude, $\tilde{\mathbf{y}} \equiv [\tilde{m}_{\text{app}} \ \tilde{a}z \ \tilde{e}]^T$. Estimated observations are computed for each sigma point using the observation models discussed previously. The mean estimated output are computed, and the output, innovations, and cross-correlation covariance are computed using the sigma points. Finally, the Kalman gain is calculated from the sigma point and is used to update the estimated state vector that contains the error GRPs. If any of the updated area states are found outside the feasible region they are projecting onto the constraint boundary. The quaternion update is performed by converting the error GRP states of $\hat{\mathbf{x}}_k^+$ to a quaternion, $\delta\hat{\mathbf{q}}_k^+$, via Eq. (41), and adding it to the estimated quaternion using quaternion multiplication.

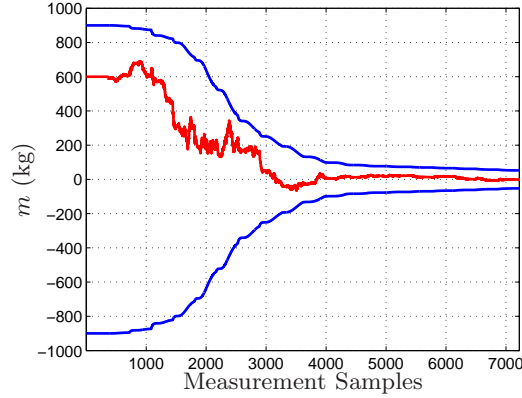


Figure 5: Mass Error Estimated Using Method I

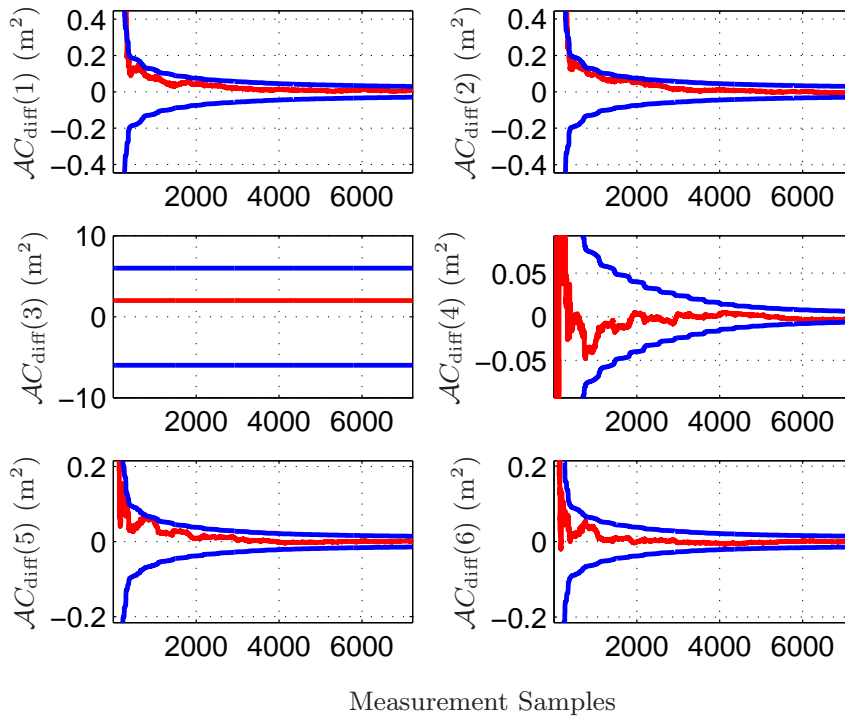


Figure 6: Albedo-Area Estimated Using Method I

4 Results

Three simulations are presented: method I is used to estimate mass using an assumed albedo value; method II is used to estimate mass and area; and a study is conducted to determine the effect of area-to-mass ratio on mass estimation performance. In all cases the same dynamic configuration is considered, with same initial attitude, true orbit and true angular velocity. For the generation of data for the true model, an equatorial ground station is chosen as the site of the observer. Also, all scenarios use the same shape model which contains six sides where the areas and albedo-areas for these sides are estimated. The SO is simulated to fly in a near-geosynchronous orbit in a trajectory that is continuously lighted. This is accomplished by inclining the orbit by 30 degrees and choosing an appropriate time of the year, thereby avoiding the shadow cast by the Earth. The simulation parameters are:

- Geographic position of the ground site is 0° North, 172° West with 0 km altitude
- Initial inertial position is chosen as $\mathbf{r}^I = [-7.8931 \times 10^2 \ 3.6679 \times 10^4 \ 2.1184 \times 10^4]^T$ km
- Initial inertial velocity is chosen as $\mathbf{v}^I = [-3.0669 \ -4.9425 \times 10^{-2} \ -2.8545 \times 10^{-2}]^T$ km/s
- The initial time of the simulation is May 8, 2007 at 5:27.55
- Initial quaternion: $\mathbf{q}_I^B = [1/\sqrt{2} \ 0 \ 0 \ 1/\sqrt{2}]^T$
- A constant rotation rate, defined as the body rate with respect to the inertial frame, represented in body coordinates, is used given by $\boldsymbol{\omega}_{B/I}^B = [0 \ 0.00262 \ 0]^T$ rad/s.

For all simulations scenarios, measurements are produced using zero-mean white-noise error processes with standard deviation of 0.1 for magnitude and standard deviation of 1 arc-seconds for azimuth and elevation. The initial errors for the states are 5 deg for all three attitudes, 1,000 deg/hr for the rotational rates, and 1 km and 0.001 km/s for the position and the velocity errors, respectively. The initial condition error-covariance values are set to 20^2 deg² for all three attitude components, $1,400^2$ (deg/hr)² for the rotational rates, and 1^2 km² and 0.001^2 (km/s)² for the position and the velocity errors, respectively. The initial condition error-covariance values for the mass, albedo-area, and area are 300^2 kg², 10^2 m⁴, and 10^2 m⁴, respectively. The time interval between the measurements is set to 30 seconds. Data is simulated for 20 nights (about 20 orbits) where observations of the SO are made each night for 3 hours. The simulation results are plotted versus number of data samples since there are large time gaps between each 3 hour data arc.

For the development of the measured light curve data a six sided facet SO shape model is used. The three parameters for the shape model are given, l , c , and d which are the length, width, and height respectively, as shown in Figure 2. For the truth model a six-facet rectangular shape model is used with dimension $l = 4$ m, $c = 2$ m, and $d = 8$ m. The mass for the true SO is selected to be $m = 1,500$ kg, which gives a maximum area-to-mass ratio of 0.09 for this model. For the area-to-mass ratio study this ratio is varied from 0.01 to 10. All facets have reflectance values of $C_{\text{spec}} = 0$ and $C_{\text{diff}} = 0.5$, under the assumption that the SO is perfectly diffuse. For method I, the assumed albedo is set to the true value $C_{\text{diff}}(i) = 0.3$ for all i .

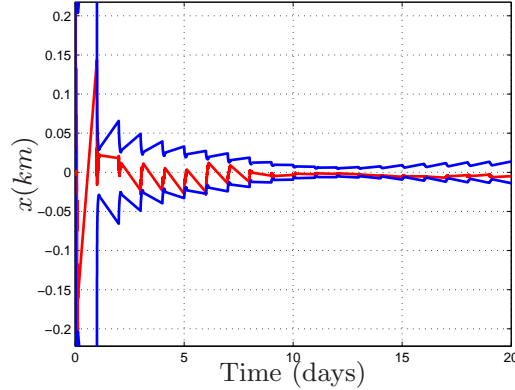


Figure 7: x Error vs. Time Method I

4.1 Angles and Magnitude Fusion: Method I

The estimation errors, along with their respective 3σ bounds calculated from the covariance for method I, for attitude, position, velocity, rotation rate, mass, albedo-areas, and areas, are shown in Figure 4. The attitude is estimated to within 0.03° of uncertainty, and attitude rate is found to within 0.05 deg/hr for the x -axis, 4.5×10^{-4} deg/hr for the y -axis (the y -axis is the spin axis), and 0.03 deg/hr for the z -axis. All error plots for all methods are shown versus measurement samples. This is done since there are large propagation periods between measurement arcs. Therefore to see the estimation error changes as measurements are processed,

plots of errors versus measurement samples are more effect. The x error is shown versus time in figure 7 and from the figure it is clear that the error increase during propagation. This increase in error is also seen in all other plots that are versus measurements in the spikes of the 3σ bounds as the error increases. Position and velocity are estimated to within 10 m and 0.0028 m/s, respectively. The mass is estimated to within 54.76 kg 3σ as shown in Figure 5, and the albedo-areas are estimated to 0.5 m^2 . For the albedo-area plot in Figure 6, the estimates are plotted going from $+x, -x, +y, -y, +z$ and $-z$. The area states are not estimated for method I since the albedo is assumed known. Also the albedo-areas plot in Figure 6 shows that the third area component ($+y$ component) is not observable. This is due to the fact that this side does not face the observer because the SO is spinning about the y -axis. Although this side is not very observable, the filter can still observe mass states. This is due to the fact the SRP disturbance is a sum of all the cross-sectional errors and overtime through the rotational dynamics of the space object, all the sides contribute to the translational dynamics, creating observability. Most states show proper filter convergence behavior in that the residual errors settle down and are bounded by their computed 3σ bounds.

4.2 Angles and Magnitude Fusion: Method II

The estimation errors, along with their respective 3σ bounds calculated from the covariance for method II, for attitude, position, velocity, rotation rate, mass, albedo-areas and areas are shown in Figure 8. The estimated attitude, attitude rate, position and velocity show similar performance to that of method I. The albedo-areas also show similar performance to that of method I and are estimated to 0.5 m^2 , as shown in Figure 9. The mass estimate for method II has larger error than that of method I, where the mass is estimated to within $200.67 \text{ kg } 3\sigma$. The area state estimates are shown in Figure 10, and the area state shows small improvement in the estimated error. Although the area uncertainty is still higher, the mass is still observable, as shown in Figure 11, and the uncertainty in the area is accounted for in method II. Most states show proper filter convergence behavior in that the residual errors settle down and are bounded by their computed 3σ bounds.

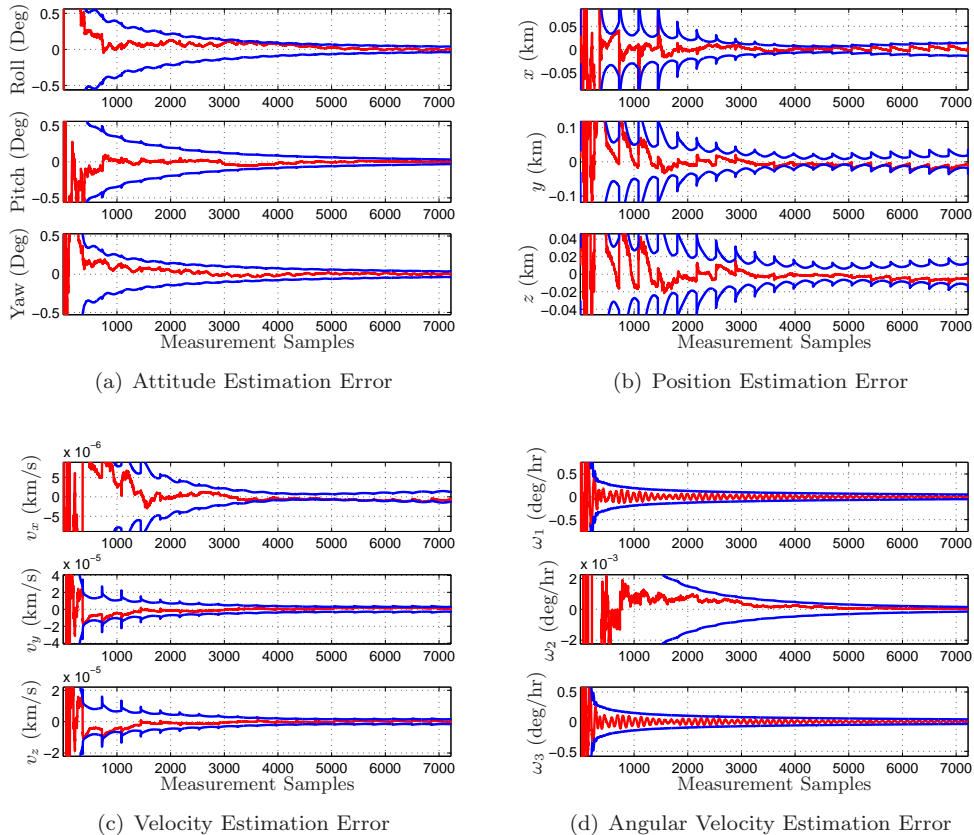


Figure 8: SO State Estimation Results for Method II

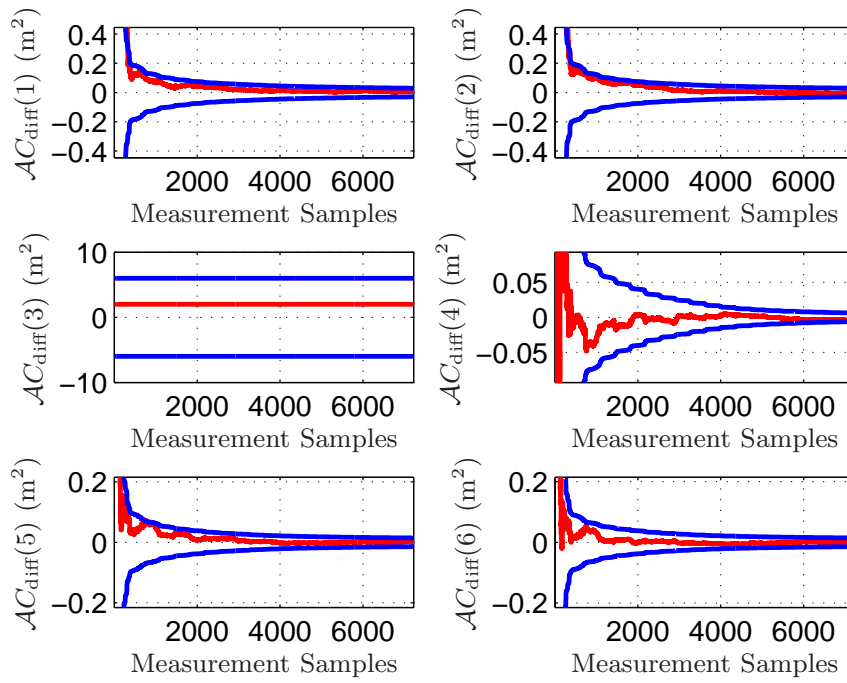


Figure 9: Albedo-Area Estimated Using Method II

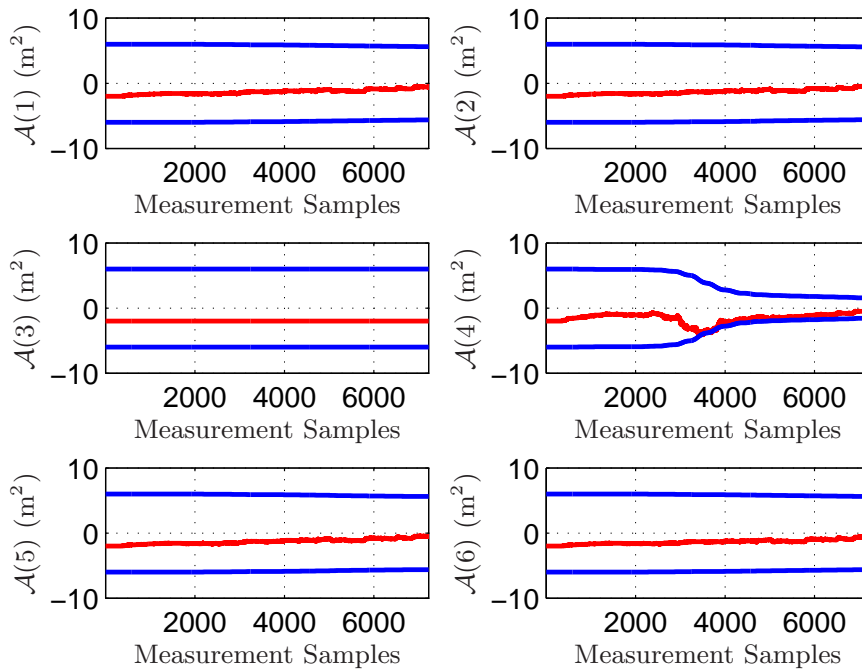


Figure 10: Area Estimated Using Method II

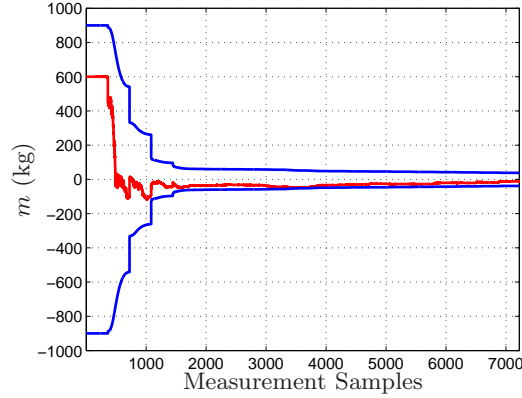


Figure 11: Mass Error Estimated Using Method II

4.3 Angles and Magnitude Fusion: Method III

The estimation errors, along with their respective 3σ bounds calculated from the covariance for method III, for rotational, translational states, mass, albedo-area and albedo are shown in Figures 12–15. The estimated attitude, attitude rate, position and velocity show similar performance to that of methods I and II. The albedo-areas also show similar performance to that of methods I and II and are estimated to 0.5 m^2 . Since method III estimates albedo, which has an upper limit of 1, the estimation process is better than method II which estimates area that may have no upper bound. The mass estimate for method III, which is estimated to within $160 \text{ kg } 3\sigma$, has larger error than that of method I but is smaller than that of method II. Most states show proper filter convergence behavior in that the residual errors settle down and are bounded by their computed 3σ bounds. Note that the albedo has values between 0 and 1.

4.4 Dependence on Area-to-Mass Ratio

To study the convergence rate of the mass estimates as a function of area-to-mass ratio, a number of simulations for conducted where A/m is varied over four orders of magnitude, $A/m = [0.01 \ 0.1 \ 1 \ 10]$. Figure 16 shows the mass estimate error covariance for the area-to-mass ratios considered. As expected, as the area-to-mass ratio increases the convergence rate also increases. This is due to the fact that for higher area-to-mass ratio objects, the effect of SRP perturbation is greater; and therefore, the mis-modeling effect appears faster in the data, making the mass and area parameters observable earlier. Also it can be seen from Figure 16 the steady state error is reduced for objects with higher area-to-mass ratios. This is due to fact that, for these class of objects, the disturbance seen from SRP is much higher than the estimated error in their translational states; the SRP disturbance is thus shown to have good signal-to-ratio characteristics. Figure 16 that the converged mass values for A/m of 0.01, 0.1, 1, and 10 are 160.12 kg, 30.45 kg, 2.71 kg, and 0.80 kg, respectively.

5 Conclusion

In this paper, an unscented Kalman filter estimation scheme using light curve and angles data was presented and was used to estimate mass, albedo-areas and areas of a SO along with its associated rotational and translational states. This work uses an assumed shape model of six sides and estimated the area and albedo-areas for each side. Using an unscented filter to employ brightness magnitude and angles data, the estimator was able to determine the mass of a SO to within $54.76 \text{ kg } 3\sigma$. Simulations were conducted to study the dependance of convergence rate and estimate accuracy on the area-to-mass ratio of the SO. Three different approaches were developed. Method I assumes an albedo value while method II does not assume an albedo value and estimates the area. Method III also does not assume an albedo value and estimates the albedo directly. Choosing which method to use depends on what a priori information is available. For example, if the albedo is known then method I should be used, or if the area and albedo is known then method II should

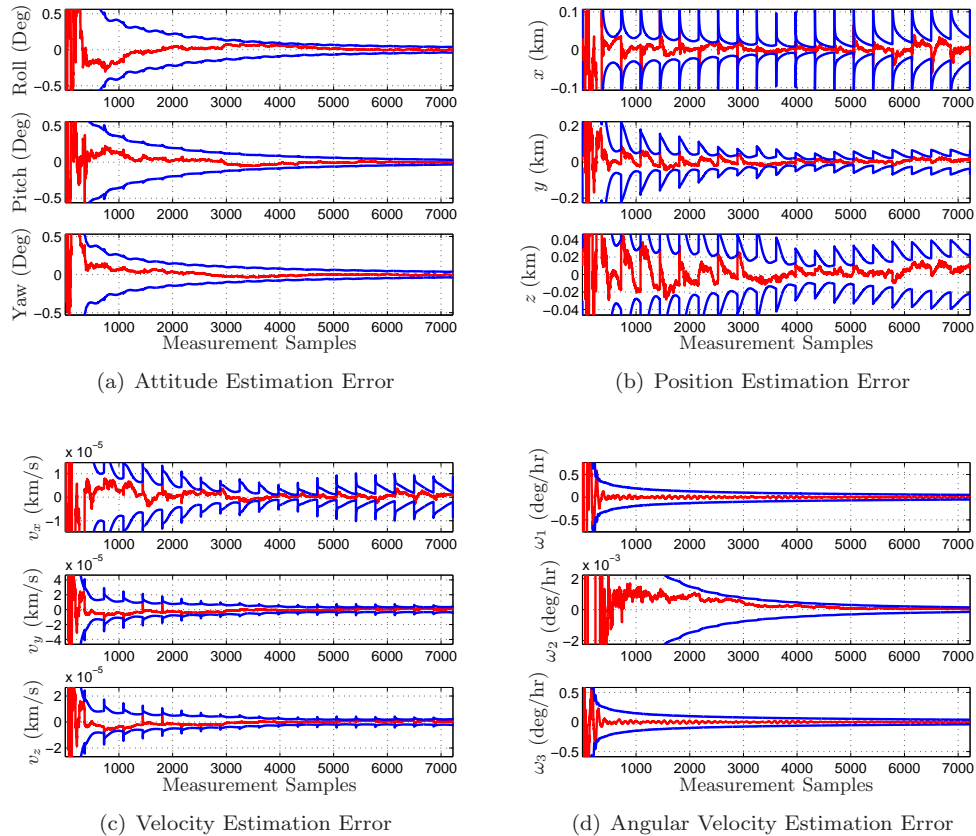


Figure 12: SO State Estimation Results for Method III

be employed. As expected, it was shown that for higher area-to-mass ratios the mass and area states could be estimated to higher accuracy with faster convergence rates.

6 Acknowledgement

This work was supported through multiple funding mechanisms, one of which was via the Air Force Research Laboratory, Space Vehicles Directorate (ASTRIA) Space Scholars Program. The support of the Space Scholars program at the AFRL Space Vehicles Directorate is gratefully acknowledged.

References

- [1] Schildknecht, T., “Optical Surveys for Space Debris,” *Astronomy and Astrophysics Review*, Vol. 14, No. 1, 2007, pp. 41–111.
- [2] Kaasalainen, M. and Torppa, J., “Optimization Methods for Asteriod Lightcurve Inversion I: Shape Determination,” *Icarus*, Vol. 153, No. 4, Jan. 2001, pp. 24–36.
- [3] Kaasalainen, M., Torppa, J., and Muinonen, K., “Optimization Methods for Asteriod Lightcurve Inversion II: The Complete Inverse Problem,” *Icarus*, Vol. 153, No. 4, Jan. 2001, pp. 37–51.
- [4] Calef, B., Africano, J., Birge, B., Hall, D., and Kervin, P. W., “Photometric Signature Inversion,” *Proceedings of the International Society for Optical Engineering*, Vol. 6307, San Diego, CA, Aug. 2006, Paper 11.

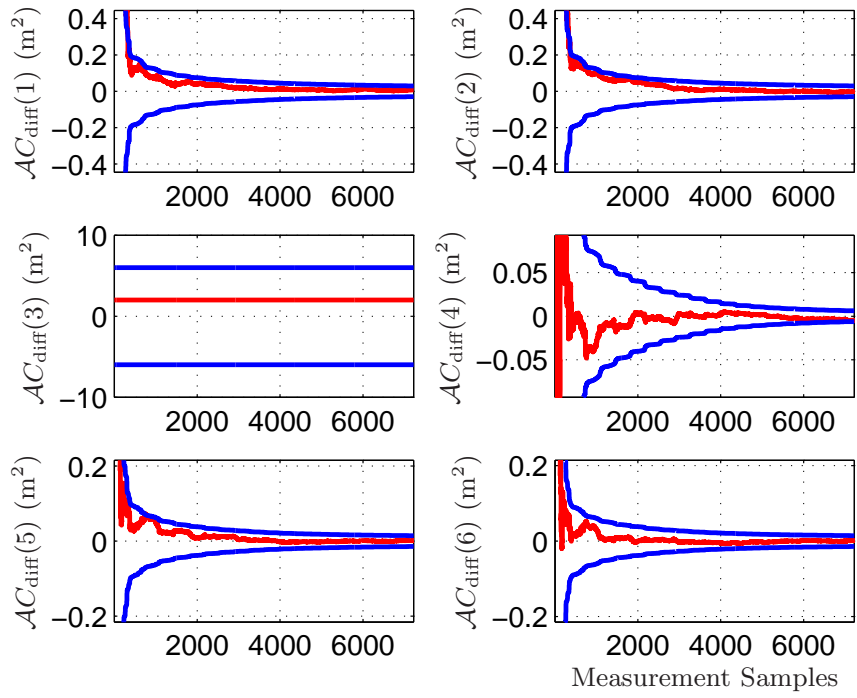


Figure 13: Area Estimated Using Method III

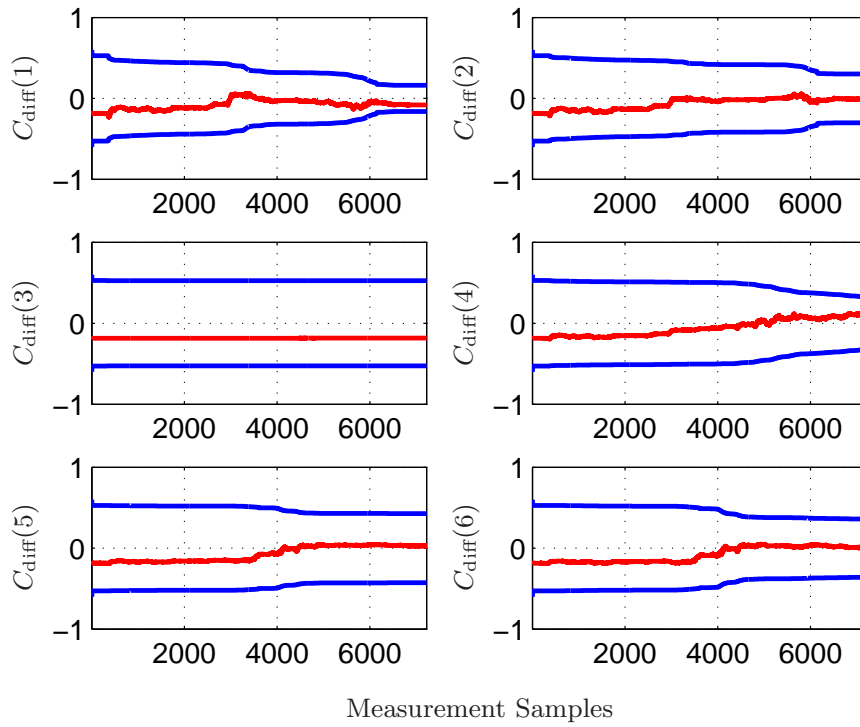


Figure 14: Albedo Estimated Using Method III

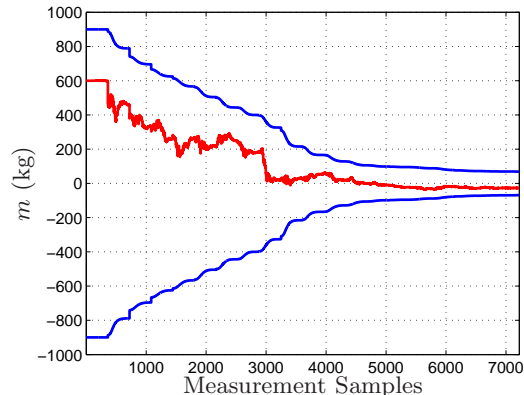


Figure 15: Mass Error Estimated Using Method III

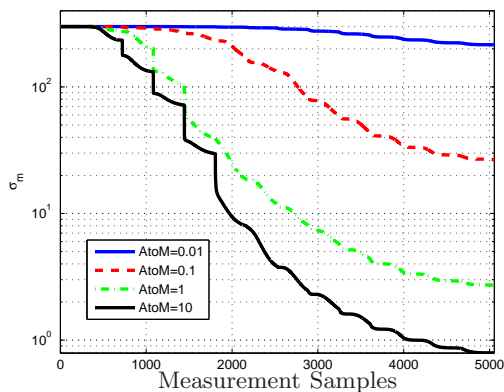


Figure 16: Mass Variance Versus Number of Data Sample for Varying Area-to-Mass Ratios

- [5] Jah, M. and Madler, R., “Satellite Characterization: Angles and Light Curve Data Fusion for Spacecraft State and Parameter Estimation,” *Proceedings of the Advanced Maui Optical and Space Surveillance Technologies Conference*, Vol. 49, Wailea, Maui, HI, Sept. 2007, Paper E49.
- [6] Centinello, F. J., “Six Degree of Freedom Estimation with Light Curve Data,” Tech. rep., Air Force Research Laboratory, Kihei, HI, 2008.
- [7] Kelecny, T. and Jah, M., “Analysis of High Area-to-Mass Ratio (HAMR) GEO Space Object Orbit Determination and Prediction Performance: Initial Strategies to Recover and Predict HAMR GEO Trajectories with No a priori Information,” *Acta Astronautica*, Vol. 69, No. 7-8, Sept. 2011, pp. 551–558.
- [8] Linares, R., Crassidis, J. L., Jah, M., and Kim, H., “Astrometric and Photometric Data Fusion for Orbit, Attitude, and Shape Estimation,” *AIAA Guidance, Navigation and Control Conference*, Chicago, IL, Aug. 2010, AIAA-2009-6293.
- [9] Jazwinski, A. H., *Stochastic Processes and Filtering Theory*, chap. 8, Academic Press, San Diego, CA, 1970.
- [10] Julier, S. J., Uhlmann, J. K., and Durrant-Whyte, H. F., “A New Method for the Nonlinear Transformation of Means and Covariances in Filters and Estimators,” *IEEE Transactions on Automatic Control*, Vol. AC-45, No. 3, March 2000, pp. 477–482.

- [11] Gordon, N. J., Salmond, D. J., and Smith, A. F. M., “Novel Approach to Nonlinear/Non-Gaussian Bayesian State Estimation,” *IEE Proceedings, Part F - Communications, Radar and Signal Processing*, Vol. 140, No. 2, Seattle, WA, April 1993, pp. 107–113.
- [12] Wetterer, C. J. and Jah, M., “Attitude Estimation from Light Curves,” *Journal of Guidance, Control and Dynamics*, Vol. 32, No. 5, Sept.-Oct. 2009, pp. 1648–1651.
- [13] Africano, J., Kervin, P., Hall, D., Sydney, P., Ross, J., Payne, T., Gregory, S., Jorgensen, K., Jarvis, K., Parr-Thumm, T., Stansbery, G., and Barker, E., “Understanding Photometric Phase Angle Corrections,” *Proceedings of the 4th European Conference on Space Debris*, Vol. SP-587, Darmstadt, Germany, April 2005, pp. 141–146.
- [14] Shuster, M. D., “A Survey of Attitude Representations,” *Journal of the Astronautical Sciences*, Vol. 41, No. 4, Oct.-Dec. 1993, pp. 439–517.
- [15] Ashikmin, M. and Shirley, P., “An Anisotropic Phong Light Reflection Model,” Tech. Rep. UUCS-00-014, University of Utah, Salt Lake City, UT, 2000.
- [16] Crassidis, J. L. and Markley, F. L., “Unscented Filtering for Spacecraft Attitude Estimation,” *Journal of Guidance, Control and Dynamics*, Vol. 26, No. 4, July-Aug. 2003, pp. 536–542.
- [17] Schaub, H. and Junkins, J. L., “Stereographic Orientation Parameters for Attitude Dynamics: A Generalization of the Rodrigues Parameters,” *Journal of the Astronautical Sciences*, Vol. 44, No. 1, Jan.-March 1996, pp. 1–20.
- [18] Kandepu, R., Imsland, L., and Foss, B. A., “Constrained State Estimation Using the Unscented Kalman Filter,” *2008 16th Mediterranean Conference on Control and Automation*, No. i, IEEE, Congress Centre, Ajaccio, France, 2008, pp. 1453–1458.